NEOPLASIA
www.neoplasia.com

Volume 11 Number 9 September 2009 pp. 889–900 889

Using Optical Spectroscopy to Longitudinally Monitor Physiological Changes within Solid Tumors[1]

Karthik Vishwanath*, Hong Yuan†, William T. Barry‡, Mark W. Dewhirst§ and Nimmi Ramanujam*

*Department of Biomedical Engineering, Duke University, Durham, NC 27708, USA; †Department of Radiology, University of North Carolina at Chapel Hill, Chapel Hill, NC 27599, USA; ‡Department of Biostatistics and Bioinformatics, Duke University, Durham, NC 27710, USA; §Department of Radiation Oncology, Duke University, Durham, NC 27710, USA

Abstract

The feasibility of using quantitative diffuse reflectance spectroscopy to longitudinally monitor physiological response to cancer therapy was evaluated in a preclinical model. This study included two groups of nude mice bearing 4T1 flank tumors ($N = 50$), half of which were treated with a maximum tolerated dose of doxorubicin (DOX). Diffuse reflectance spectra were collected from tumors during a period of 2 weeks using a fiber-optic probe coupled to a spectrometer. These spectra were quantified using an inverse scalable Monte Carlo model of light transport in tissue to extract the concentrations of oxygenated, deoxygenated hemoglobin (dHb), and a wavelength mean reduced scattering coefficient ($<\mu_s'>$). The tumor growth rates of the treated and control groups were nearly identical, as were changes in the scattering parameter $<\mu_s'>$ during this time frame. However, tumors treated with DOX showed a transient but significant increase in blood oxygen saturation. A comparison between the optically derived and immunohistochemical end points in a subset of the 50 animals showed that the temporal kinetics of dHb concentration and $<\mu_s'>$ were highly concordant with those of hypoxic and necrotic fractions, respectively. In conclusion, optical methods could function as a "screening" technology in longitudinal studies of small animal tumor models to accelerate development and testing of new anticancer drugs. This technique could isolate specific landmark time points at which more expensive and sophisticated imaging methods or immunohistochemistry could be performed.

Neoplasia (2009) 11, 889–900

Introduction

Preclinical animal models are widely used in studies seeking to understand cancer biology, particularly, tumor growth, and metastatic behavior [1]. Animal tumor models have provided a template for researchers to understand the genetic basis of molecular pathways involved in tumorigenesis, elucidate the detailed understanding of drug delivery and transport in solid tumors, and investigate the effects of novel therapeutic regimens [2,3]. For decades, the standard method for evaluating the merits of new therapeutic agents in preclinical models has been the standard tumor growth delay assay. This method quantifies the growth rates of control and treated tumors to determine whether a new therapeutic regimen provides any slowing of growth compared with controls. Although this method has been valuable, it hides a plethora of pathologic and physiologic changes that occur in treated tumors that could have important therapeutic implications. A case in point involves "vascular targeting drugs," such as combrestatin A4. These compounds cause substantial damage to tumor microvasculature within a few minutes of administration [4] and can lead to complete necrosis of the central portions of a tumor within hours [5]. However, a standard growth delay method exhibits no therapeutic advantage to giving these drugs because the cells at the tumor–normal tissue boundary repopulate

Abbreviations: dHb, deoxygenated hemoglobin; DOX, doxorubicin; IHC, immunohistochemistry; MTD, maximum tolerated dose; μ_s', mean reduced scattering; HbO_2, oxygenated hemoglobin; MC, Monte Carlo

Address all correspondence to: Karthik Vishwanath, Department of Biomedical Engineering, 136 Hudson Hall, Box 90281, Duke University, Durham, NC 27708.
E-mail: kvh1@duke.edu

[1]Funding support for this work was provided by a Department of Defense Era of Hope Scholar award (W81XWH-05-1-0363) and by a National Institutes of Health grant (R01 CA40355-23).
Received 6 April 2009; Revised 11 June 2009; Accepted 12 June 2009

DOI 10.1593/neo.09580

the tumor very rapidly, aided by a rapid influx of endothelial cell progenitors that promote rapid recovery of angiogenesis [6]. Similarly, it has been shown that inhibition of the hypoxia-inducible factor (HIF-1) causes profound metabolic stress on hypoxic cells because HIF-1 is responsible for upregulating nearly all of the genes involved in anaerobic metabolism [7]. Glucose is the only viable energy substrate for hypoxic cells; thus, in the absence of HIF-1, these cells starve to death, leaving only a small viable rim of tumor cells growing at the margin of the original tumor. Yet, on using a standard growth delay method to evaluate the effects of HIF-1 inhibition, it has been shown that there was virtually no effect on growth delay because growth at the tumor margin hid the underlying changes in tissue physiology and pathology [7]. It is therefore important to assess the underlying tumor physiological and pathologic changes to improve treatment efficacy.

One such important parameter that influences tumor growth, metabolism, treatment resistance, and metastatic behavior is tumor hypoxia or low oxygen tension [8,9]. Tissue hypoxia is definitively diagnosed using immunohistochemical assays that directly detect intrinsic markers of hypoxia (such as carbonic anhydrase IX, osteopontin, or HIF-1) or relies on the use of extrinsic agents (such as pimonidazole or EF5) to selectively stain hypoxic cells [10]. A standard nonhistologic method to measure hypoxia is electrode polarography; this yields point measurements of P_{O_2} (sampled from ~100 to 300 cells) at spatial locations along the path of electrode insertion and withdrawal within the tissue [11]. Tissue oxygen concentrations have also been assessed using perfluorinated compounds in combination with electron paramagnetic resonance spectroscopy, indirectly using 2-nitroimidazoles with positron emission tomography (PET) and magnetic resonance (MR) spectroscopy [10].

Another parameter used to assess the efficacy of cancer therapies involves alterations in tumor morphology and structure including cellular and nuclear features of shape, size, crowding, chromatin organization, and DNA structure [12]. This is most commonly done using histopathologic and immunohistochemistry (IHC) techniques. These methods identify two important features of cell death, namely, apoptosis and necrosis, both of which have the ability to predict disease-free survival in patients after therapy [13–15]. Alternately, PET and MR imaging (MRI) have been applied to noninvasively detect cell death *in vivo*. MRI measures of the apparent diffusion coefficient of water in tissue can provide information regarding tissue structure from the water content present in the intracellular and the extracellular space, which in turn can be used to assess cell death occurring through necrosis or apoptosis [16,17]. Conversely, PET imaging methods for sensing apoptosis and/or necrosis rely on using labeled apoptosis or necrosis markers such as ^{18}F-labeled annexin V [17].

Studies seeking to quantify changes in physiology including tumor hypoxia and/or cell death using IHC face logistical challenges because these methods require killing animals at regularly spaced intervals to assay them. Moreover, longitudinal studies involving IHC cannot repeatedly track individual subjects because the measurement of an individual using IHC techniques necessitates the loss of the subject. Both these constraints lead to the requirement of large sample sizes to draw meaningful conclusions about a particular therapy. Alternate high-resolution, sophisticated, and noninvasive imaging techniques such as MRI or PET can repeatedly obtain serial measurements on individual subjects, but they have high associated operating costs and may not always be amenable to frequent use in small animal studies.

Here, we present an optical spectroscopic approach to nondestructively and dynamically quantify changes in several key biomarkers of carcinogenesis, specifically, tumor oxygenation and cellular morphology (necrosis, in particular) in preclinical tumor models. Our technology is based on diffuse reflectance spectroscopy that quantifies the wavelength dependence of the reflected light after it has undergone absorption and scattering interactions in the tissue [18–20]. Primary absorbers in soft tissues include oxygenated hemoglobin (HbO_2) and deoxygenated hemoglobin (dHb), both of which indicate blood oxygenation status of the tissue. Tissue scattering contains information about the underlying cellular architecture, is sensitive to the size and density of cellular and subcellular structures such as nuclei and mitochondria, and can be altered by cell death and/or cell proliferation. The sensing depth offered by diffuse reflectance spectroscopy depends on factors that include the source-detector geometry used to deliver and collect the light and the optical properties (absorption and scattering) of the interrogated tissue. Because both the optical absorption and scattering of most tissues decrease with increasing wavelength, the penetration depth of light increases from a few millimeters in the UV-visible spectrum to several centimeters in the near-infrared (NIR). Our technology is designed to be used in the visible spectral range, which provides a sensing depth in the millimeter range and is comparable to the size of tumors in preclinical models such as nude mice. Traditionally, quantitative extraction of absorber concentrations (which yield information on the blood oxygen status and total blood concentration) and tissue scattering are typically obtained using closed-form analytical expressions of light transport in turbid medium, which are best suited for use in the longer, NIR spectral range [21]. We have developed a series of computational Monte Carlo (MC) algorithms that can quantitatively extract tissue absorption and scattering *in vivo* [22] while accurately accounting for the fiber probe geometry over a wide wavelength range including the visible and NIR. Unlike the closed-form analytical expressions, these computational models are well suited to the visible spectral regime and for small source-detector separations as is proposed for use on tumors in small animal models.

This article focuses on the use of visible diffuse reflectance spectroscopy in characterizing changes in optical parameters related to tumor hypoxia and necrosis *in vivo* in a preclinical model of breast cancer. 4T1 breast tumors were grown in the flank of nude mice, and the animals were separated into control and treatment groups and monitored optically during a 2-week period. The treated animals received a maximum tolerated dose (MTD) of doxorubicin (DOX). These diffuse reflectance spectra were then processed through a quantitative MC model developed by our group [22] to extract the concentrations of HbO_2 and dHb in blood within the tumor vasculature along with an associated reduced scattering coefficient spectrum. Tumors from animals in both groups were also resected at four time points for IHC analysis of hypoxic and necrotic fractions. The main findings from our study were as follows: Treatment with MTD DOX showed no differences in the standard growth delays between the treated and untreated tumors. However, tumors treated with DOX showed a transient but significant increase in blood oxygen saturation, which is consistent with previously published studies [23]. A comparison between the optically derived and IHC end points showed that the temporal kinetics of dHb concentration and the reduced scattering coefficient were highly concordant with those of hypoxic and necrotic fractions, respectively.

Materials and Methods

Animal Study Protocol

Fifty nude mice with a mean ± SD weight of 20.7 ± 3.2 g were ordered from the National Cancer Institute (Bethesda, MD) and stored at

the Duke animal facility in a 12-hour dark-light cycle. Food and water were allowed *ad libitum*. Approximately, 10^6 4T1 mouse breast carcinoma cells suspended in 0.1 ml of serum-free medium were inoculated subcutaneously in the right flank of the animals. Once the tumor diameter reached 4 to 6 mm, the animals were evenly distributed (by tumor size) into control and treatment groups (each group had 25 animals). The treatment group received an MTD dose of DOX (10 mg/kg, intravenously using a previously prepared solution of 2-mg/ml DOX), whereas the control group received an equivalent volume of saline. These studies were approved by the Duke Institutional Laboratory Animal Care and Use Committee.

The tumors were monitored optically before treatment to get baseline measurements (day 0) and then on days 2, 5, 7, 10, and 13 after DOX or saline administration. The animals were maintained under anesthesia by isoflurane breathing (1.5% isoflurane gas mixed with oxygen) throughout the course of the optical measurements. Five randomly chosen animals, from each group, were removed for IHC on days 0, 5, 10, and 13. These treatment schedules and time points were selected from previous pilot studies that showed maximal differences in the optical end points between the treated and the control groups. The tumors from the animals designated for IHC were resected, snap-frozen by placing the tumor in a container immersed in liquid nitrogen, and stored for subsequent histologic diagnosis and IHC. For each of these animals, the outline of the fiber-optic probe was traced on the surface of the tumor immediately after the optical measurement to ensure that the resected tumors could be sectioned as closely parallel to the face of the fiber-optic probe as possible, thereby yielding sections from nearly the same tissue volumes as sensed by the optical measurements.

Immunohistochemistry

The harvested, snap-frozen tumors were sliced into 10-μm-thick sections using a cryotome (CM1850; Leica, Inc., Nussloch, Germany). The orientation of the resected tumor on the microtome before sectioning was determined from the marked circle on the tumor surface that indicated the outline of fiber-optic probe position such that the sections were parallel to the face of the optical probe. For each tumor, five sections were obtained from depths of 600 μm and 1.6 mm below the surface. Slides were counted from the start of cutting and were numbered consecutively so that the depth of each section from the surface could be computed.

The hypoxic fraction for each section was determined using pimonidazole and the necrotic fractions were assessed using hematoxylin and eosin (H&E) staining. Pimonidazole as the hypoxia marker was immunostained using a direct labeling protocol: pimonidazole was injected intraperitoneally (at a dose of 60 mg/kg, from a solution of 10-mg/ml pimonidazole) 30 minutes before the animals were killed. The resected tumor sections were fixed in cold acetone for 15 minutes and blocked in donkey serum blocking reagent. The primary antibody to pimonidazole (Hypoxyprobe-1 kits; NPI, Inc, Burlington, MA) was labeled with a fluorescent immunoglobulin G probe (no. Z25005; Molecular Probes, Eugene, OR) and then incubated with tumor sections for 1 hour at room temperature, washed with phosphate-buffered saline, and fixed with 10% buffered formalin for 1 minute. Stained tumor sections were kept in 1% formaldehyde phosphate-buffered saline and imaged within 3 to 4 days. After imaging, the sections were stained with H&E to allow visualization of histologic structure and quantify necrotic fraction.

Quantification of Hypoxic and Necrotic Fractions

The hypoxic fraction was determined using pimonidazole-stained images. Theoretically, pimonidazole staining is substantially increased when the intracellular oxygen tension falls to less than 10 mm Hg [24]. A higher intensity level of the fluorescence staining indicated higher hypoxia in the tissue. Imaged areas whose intensity levels were higher than a given fixed threshold were marked hypoxic, and the hypoxic fraction was calculated as a percentage area of vital tissue with the necrotic areas excluded. Because each resected mass had sections from depths of 600 μm and 1.6 mm, the hypoxic fraction for the tumor was the averaged value from both sections.

The necrotic fractions were quantified using H&E-stained sections. The necrotic areas were characterized by higher eosin staining, dark and condensed nuclei debris, and incomplete cell shapes. The necrotic fraction was calculated as the ratio of the necrotic area to the overall tissue area across each section. As before, because there were two sections corresponding to two different depths for each tumor, the averaged values were considered as the necrotic fraction for a given tumor.

Diffuse Reflectance Spectroscopy

A fiber-optic–based spectrometer (SkinSkan; JY Horiba, Edison, NJ) was used to measure diffuse reflectance spectra from the tumors. This instrument used a 150-W xenon lamp as the source, its light was filtered through a double-grating excitation monochromator for delivery, and an emission monochromator was coupled to a photomultiplier tube for light detection. The illumination and collection of the light to tissue were achieved through a bifurcated fiber-optic probe (Figure 1*B*), consisting of a central collection core of 29 fibers (arranged circularly within a diameter of 1.52 mm) surrounded by 30 illumination fibers (arranged nearly concentric to the central core with an outer diameter of 2.18 mm), where each individual fiber was 200 μm in diameter [22]. Diffuse reflectance spectra were measured between 350 and 600 nm by gently pushing the probe to make contact with the tumor surface and held fixed by a clamp throughout the course of the optical measurements. The diffuse reflectance at each wavelength was collected by integrating the signal on the photomultiplier tube for 0.1 second. The acquired spectra were calibrated by dividing the tissue diffuse reflectance spectrum by the diffuse reflectance spectrum obtained from a 99% reflectance Spectralon standard (SRS-99-020; Labsphere, Inc, North Sutton, NH) to account for variations in system throughput and wavelength response of the instrument.

Extraction of HbO_2, dHb, and μ_s'

Two measurements of diffuse optical reflectance spectra were collected from each animal on each measurement day, consecutively. These reflectance spectra were analyzed using the inverse MC model developed by our group [22] to extract wavelength-dependent absorption and scattering coefficient spectra; here, the tissue absorption/scattering coefficient is defined as the inverse mean free path for a photon (of given wavelength) to undergo an absorption/scattering event during propagation in the tissue. The tissue absorption coefficient was assumed to have contributions from HbO_2, dHb, and skin (extinction coefficients for these absorbers were obtained from a previously tabulated database [25]), whereas the scattering coefficient was calculated using a Mie theory model for spherical scatterers [22]. The following parameters were derived from the absorption and scattering coefficient spectra extracted using the inverse MC model: concentration of HbO_2, concentration of dHb, a skin-related absorption factor [26], and the reduced scattering spectrum, which, when averaged, gave a wavelength mean reduced scattering coefficient $\langle\mu_s'\rangle$ [22]. The mean value of each parameter was computed from the two sets of measured diffuse reflectance spectra, for each animal, on each measurement day.

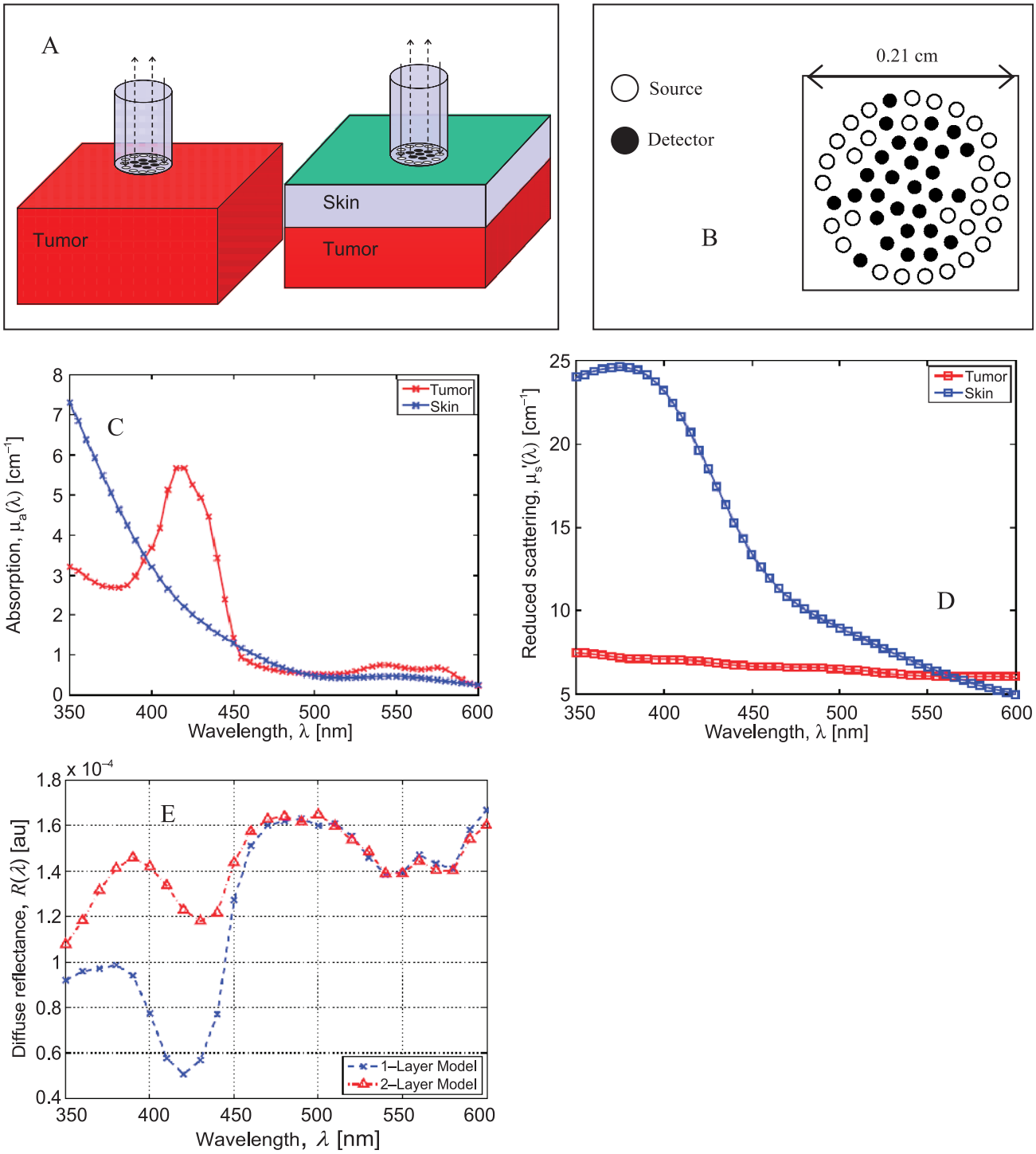

Figure 1. The tissue models, fiber probe schematic, the absorption and scattering coefficients of skin and tumor used in the modeling studies, and the predicted diffuse reflectance spectra. (A) Tissue geometries with and without a skin layer (0.3 mm). (B) Schematic of the composite probe used in these simulations and experiments. (C) Absorption coefficient spectra for the tumor (red crosses) and skin layers (blue crosses). (D) Scattering coefficient spectra for the tumor (red squares) and skin layers (blue squares). (E) Simulated diffuse reflectance spectra for the single-layer model (blue crosses) and the two-layered model (red triangles).

The extracted HbO_2 and dHb concentrations were used to compute two additional tissue physiological parameters: the total hemoglobin concentration, [THb] = [HbO_2] + [dHb]; and the oxygen saturation, SO_2 = 100 × [HbO_2] / [THb]. The wavelength range used for data analysis was 480 to 600 nm. This range was selected based on some systematic modeling studies described in the next paragraphs.

The inverse MC model [22] assumes that the interrogated tissue is an optically homogeneous, semi-infinite, turbid medium. However, the experimental measurements are better represented by a two-layered tissue model with a layer of skin covering the underlying tumor, as shown schematically in Figure 1*A*. To ascertain that we were sensitive to the underlying tumor physiology without being confounded by the presence

of the skin layer, we conducted a series of simulations using standard forward MC simulations [27] for two cases: 1) for a semi-infinite homogeneous tissue model (representing the tumor) and 2) for a two-layered tissue model that included a 300-μm-thick layer of skin atop the semi-infinite tumor, as shown in Figure 1*A*. These simulations allowed us to estimate perturbations in the diffuse reflectance spectra due to the presence of the skin layer. The skin layer thickness was set to 300 μm in these simulations because the mean ± SD skin thickness in five animals bearing 4T1 tumors was histologically measured to be 290 ± 60 μm. Forward MC simulations were computed for the two tissue models mentioned previously to generate the diffuse reflectance spectrum between 350 and 600 nm at intervals of 10 nm to simulate experimental measurements. It is to be noted that these simulations considered the exact fiber probe geometry shown in Figure 1*B* for calculations following the procedure outlined previously [22]. Figure 1, *C* and *D*, shows representative wavelength-dependent optical absorption and scattering coefficients of each layer, respectively, used in these simulations. The optical properties (absorption and scattering coefficients) of mouse skin were obtained from previously tabulated data [28], whereas those of the tumor were obtained from the results of an inversion procedure from a randomly selected animal in this study. These modeling studies considered the exact geometries of the source-detector fiber pairs of the composite fiber-optic probe to accurately compute the diffuse reflectance for the tissue model, as described elsewhere [22]. Figure 1*E* shows the simulated diffuse reflectance data for the single-layer (*blue crosses*) and the two-layered tissue models (*red triangles*). The presence of the skin layer strongly perturbed the measured diffuse reflectance spectra for wavelengths below 450 nm, whereas for wavelengths above 480 nm, the diffuse reflectance spectra for both models were quite similar. We therefore estimated that the effect of the skin layer on the measured diffuse reflectance was small in the spectral region between 480 and 600 nm and thus used the diffuse reflectance spanning 480 to 600 nm for all extractions of the absorption and scattering coefficients of the tissue.

Statistical Methods

To examine the profiles of optical parameters over time, a longitudinal mixed-effects model was applied to these end points as a common method for analyzing repeated-measures data from mouse xenografts models [29,30]. A log transformation was required to stabilize the variance and obtain residuals that were normally distributed for the optical estimates of [dHb], [THb], and $<\mu_s'>$ (data not shown). The covariance structure was estimated using a compound symmetric model that was determined to be optimal by the Bayesian information criteria. The significance of fixed effects (i.e., treatment [Controls *vs* DOX], time point [day], and their interactions) was determined in a step-up fashion using likelihood ratio tests under maximum likelihood estimation. Analyses were performed using R version 2.8.1 (www.r-project.org). For all tests, statistical significance was set at $P < .05$.

Results

Intratumor versus *Intertumor Variability in the Extracted Optical End Points*

To assess variations in each of the extracted optical end points within each animal due to spatial sampling of the tumor relative to the variation in these end points across tumors in different animals, diffuse reflectance spectra were obtained from five different spatial locations on the tumor for each animal of a total of four randomly selected animals (two treated and two control animals) on day 14. The mean coefficients of variation for the optical parameters (calculated using the five measurements per animal) within an animal were compared with the coefficient of variation computed for the 10 remaining animals on day 14 (the other 40 animals were previously killed for IHC). These data are tabulated in Table 1 and show that the interanimal coefficient of variation was significantly greater than intra-animal values for all extracted optical parameters.

Table 1. Intertumor *versus* Intratumor Coefficient of Variation in the Extracted Optical End Points.

Optical End Point	HbO_2	dHb	$<\mu_s'>$
Mean coefficient of variance within animal (n = 4)	0.26 (0.04)	0.21 (0.11)	0.12 (0.04)
Coefficient of variance across animals (n = 10)	0.62	0.67	0.21

Values in parenthesis indicate the SD in the coefficient of variance (computed across the four animals).

Representative Optical Absorption and Scattering Spectra

Figure 2 shows the diffuse reflectance spectra, the extracted absorption, and reduced scattering spectra for two representative animals (one treated and one control animal) on each measurement day until day 10. Figure 2, *A* and *B*, shows the measured diffuse reflectance spectra (symbols) and the corresponding MC model fits (lines) for one representative treated animal (Figure 2*A*, *blue symbols*) and one control animal (Figure 2*B*, *red symbols*). As seen in these figures, the model fit the measured data well (with mean residual errors <3%). Figure 2, *C* and *D*, shows the extracted absorption coefficient spectra for the treated (*blue symbols*) and control animals (*red symbols*), whereas Figure 2, *E* and *F*, shows the reduced scattering coefficient spectra for these animals, respectively. The absorption spectra on day 0 for both animals indicate that the tumors in both animals were poorly oxygenated at baseline because it is well known that the absorption coefficient (between 480 and 600 nm) of dHb exhibits a single peak at 550 nm, whereas the absorption coefficient of HbO_2 contains two absorption bands (called the α and β bands with peaks at 575 and 540 nm, respectively). By day 5, the tumor in the treated animal became progressively more oxygenated with time as seen by the growth of the characteristic α/β bands of HbO_2, whereas the tumor in the control animal continued to show a prominent single absorption band of dHb. However, the THb (which is proportional to the magnitude of the absorption coefficient) clearly increased in both animals with time. The overall shapes in the scattering coefficients for either animal are featureless, relative to the absorption spectra, but both animals showed general increases in mean scattering values with time.

Longitudinal Trends in the Optical and Tumor Volume End points

Figure 3 shows the temporal kinetics of the concentration of HbO_2 (Figure 3*A*), concentration of dHb (Figure 3*B*), the oxygen saturation (SO_2; Figure 3*C*), the THb concentration (Figure 3*D*), the mean reduced scattering coefficient ($<\mu_s'>$; Figure 3*E*), and the tumor volumes (Figure 3*F*) extracted from the data shown in Figure 2 for both animals. The *blue asterisks* show the data for the treated animal, the *red circles* show the control animal, whereas the error bars correspond to the SD between the two successive reflectance scans obtained from each animal at each time point. These data more clearly isolate the changes observed in Figure 2.

Figure 4 shows these longitudinal variations, for each optical end point (Figure 4, *A*–*E*) and tumor volume, across all treated animals (*blue*

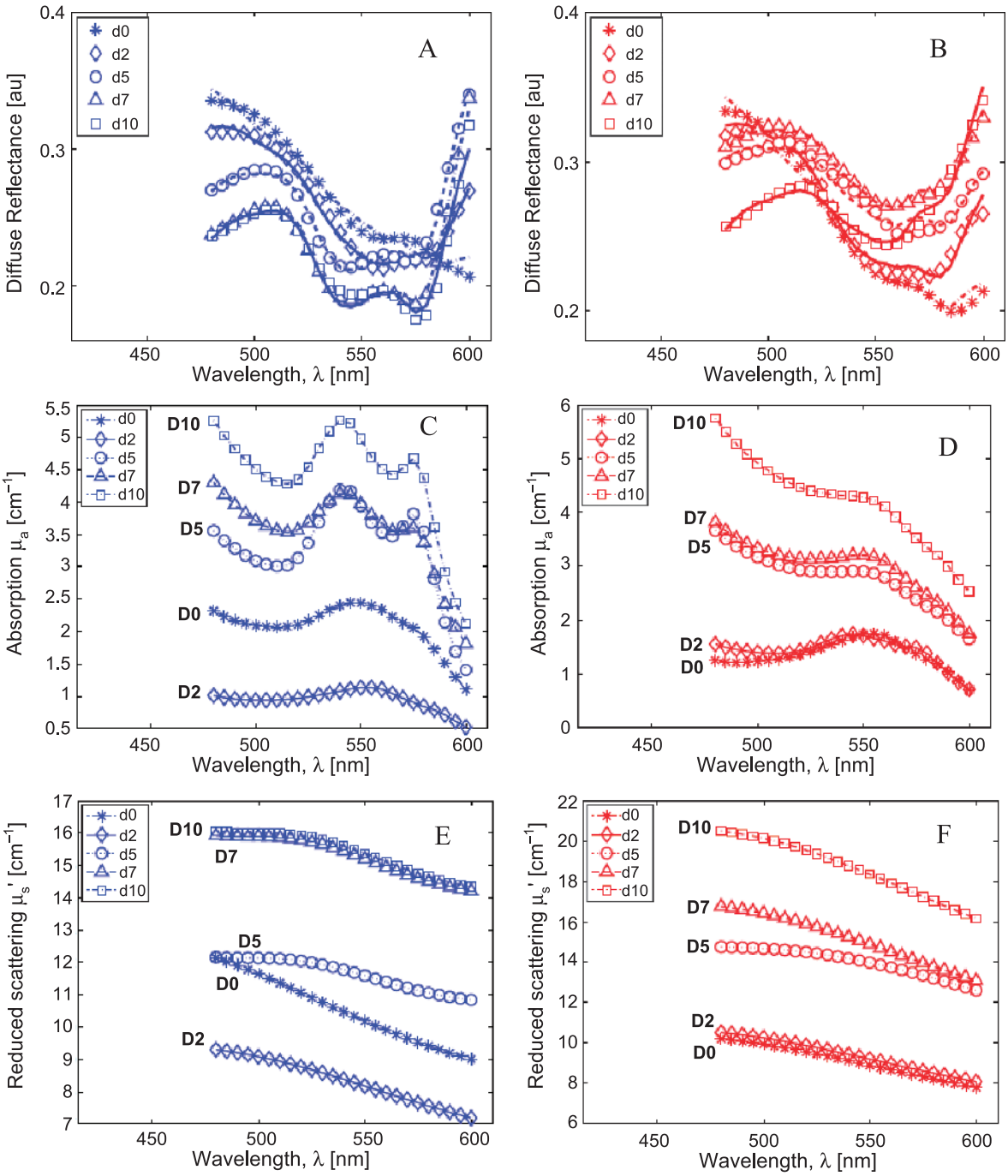

Figure 2. The measured (symbols) and fitted (lines) diffuse reflectance spectra for a representative treated (A, blue symbols) and control (B, red symbols) animal during the first 5 days. Data are shown up to day 10 because these animals were killed for IHC on day 10 (see text). Extracted absorption (C and D) and reduced scattering coefficient spectra (E and F) for the treated (blue symbols, C and E) and the control (red symbols, D and F) animals.

bars) and across all control animals (*red bars*). The numbers above the bars in Figure 4*A* represent the total number of animals that were evaluated for each group at that time point. A regression line fitted to all available longitudinal data for each end point across time per group is also shown in Figure 4 (*blue lines* indicate trends for treated animals; *red lines*, trends for controls). Figure 4*A* shows that treatment with DOX increases the mean concentration of HbO_2 across time within the tumors of the treated group relative to the animals in the control group. A similar increase in the mean SO_2 values was observed in the treated tumors relative to that in the control group (Figure 4*C*). Treatment with DOX also caused the treated tumors to have decreased dHb over time (Figure 4*B*) relative to the control group. The regression lines in Figure 4, *D* and *E*, indicate that the both [THb] content as well as $\langle \mu_s' \rangle$ changed nearly identically across time in both the treated and the control groups. Figure 4*F* shows similar rates of tumor growth for both groups.

To examine whether any of the optical end points showed an effect specifically due to treatment, a longitudinal mixed-effects model was applied to the repeated measures of all end points. These analyses indicated

that that the plotted linear trends were significantly different between the treated and the control groups for two of the six variables: treatment with DOX showed significant increases in [HbO_2] ($P = .01$) and improved tumor SO_2 ($P < .001$) in the treated tumors, relative to the tumors in the control group. The trends for [dHb] showed that the treated group had lower dHb levels relative to the controls, but they were not statistically significant ($P = .25$).

Immunohistochemical Staining

Figure 5 shows a panel of representative images from six tumor sections that were stained using Hoechst and pimonidazole. The sections shown were obtained from three different animals at each of the three different time points (*columns from left to right* show data on days 0, 5, and 10) for each of the two groups (*top and bottom rows* show data for control and treated animals, respectively). The animals shown on

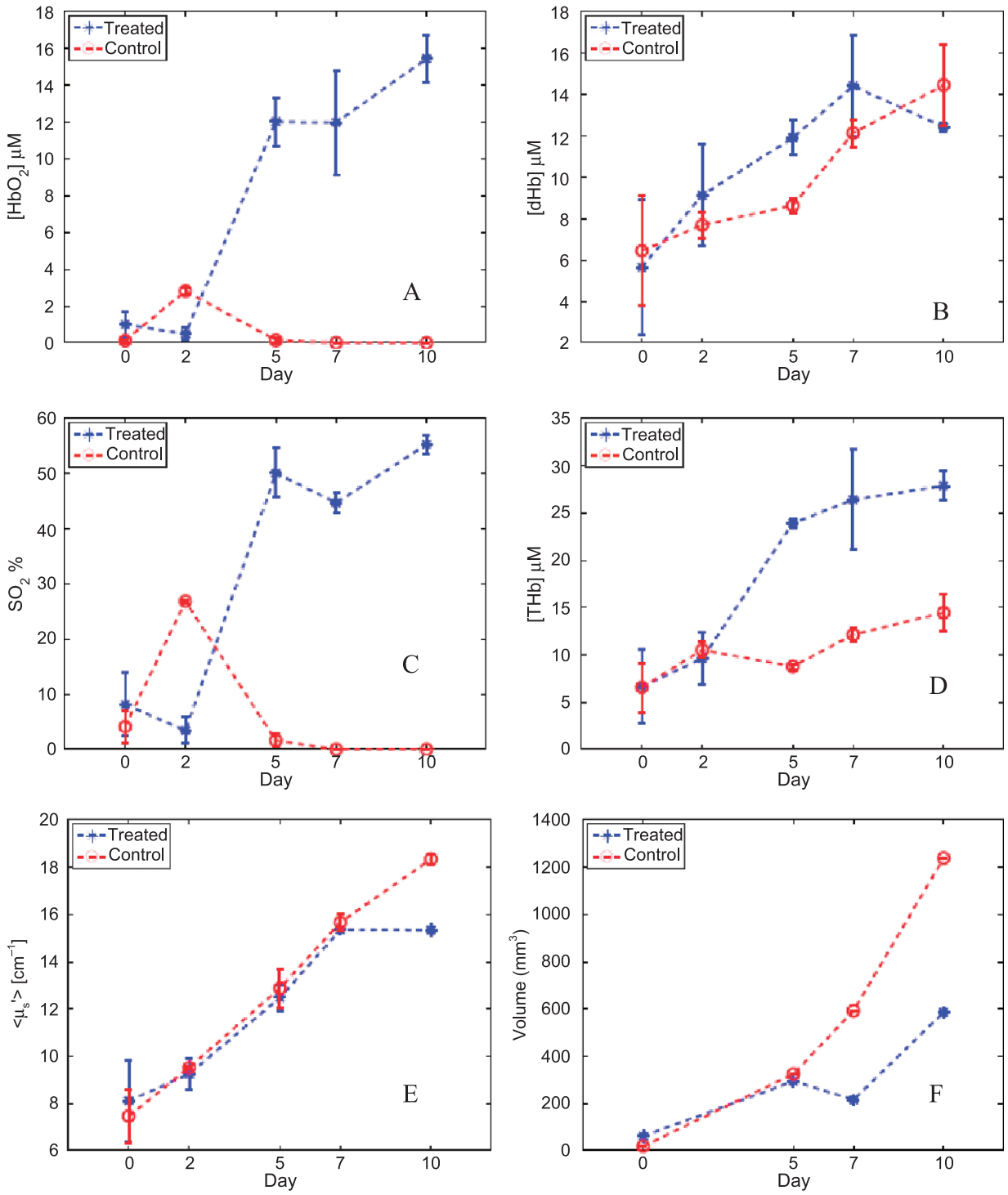

Figure 3. Temporal kinetics of [HbO_2] (A), [dHb] (B), SO_2 (C), [THb] (D), $<\mu_s'>$ (E), and tumor volumes (F) for the same animals shown in Figure 2. The blue asterisks show the data for the treated animal and the red circles show the control animal. The symbols represent the mean value obtained from the spectra obtained from two consecutive scans of the diffuse reflectance. Error bars indicate SD.

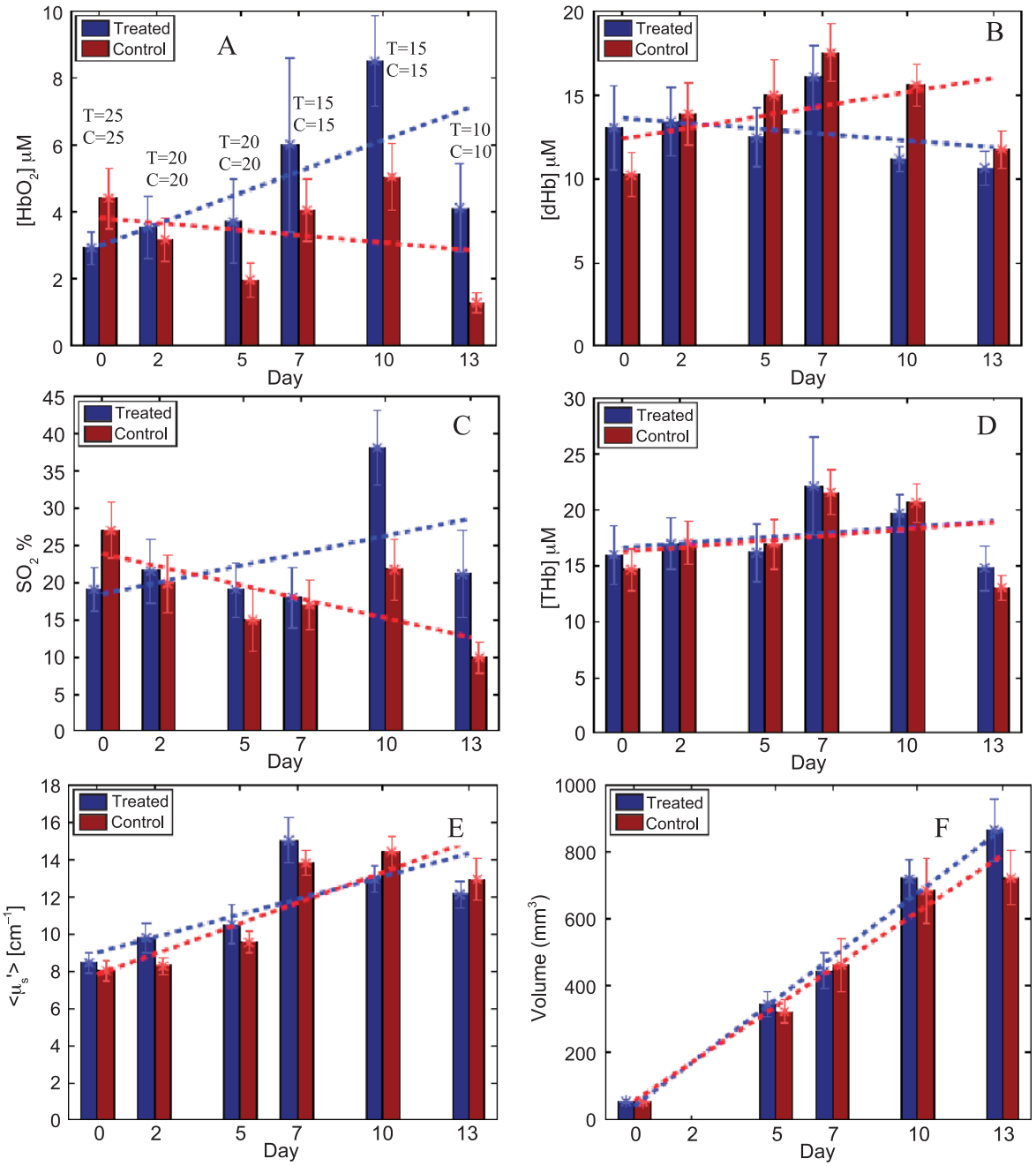

Figure 4. Longitudinal variations in all end points for each group across time: [HbO_2] (A), [dHb] (B), SO_2 (C), [THb] (D), $\langle\mu_s'\rangle$ (E), and tumor volume (F). Bars indicate mean values for each end point computed across all available animals (shown above each data bar for each day in panel A), at each particular time point, per group. Vertical lines on each bar are SEs. The dashed lines are lines of regression computed over all optical measurements across time using all available animals (at that time point) in each group (blue line indicates treated data; red line, control data).

day 10 here correspond to the treated and control animals whose optical data were shown in Figures 2 and 3. *Blue* marks Hoechst-33342 fluorescence (indicating perfused areas within the sections), whereas *orange*-stained areas show pimonidazole antibody binding (marking the hypoxic tissue area). The *dark regions* in these figures were classified either as necrotic (using corresponding H&E-stained sections; data not shown) or as nonperfused viable tissue. These data indicate that the hypoxic fraction for the control group was higher on day 10 compared with day 0, whereas these trends were reversed in case of the treated animals in these representative set of images.

Concordance between Optical and IHC End Points

The time course of changes in the IHC end points, hypoxic and necrotic fractions, were compared against the time course of changes in the most closely associated optical end point and are shown in Figure 6. Similar trends were observed between hypoxic fraction and dHb concentration (Figure 6, *A* and *B*) and between the necrotic fraction and $\langle\mu_s'\rangle$ (Figure 6, *C* and *D*) for animals from either group. It should be noted that the optical end points shown here were obtained using only five mice per group that underwent IHC at each time point and thus do not include the full sample size shown in Figure 4. To quantitatively

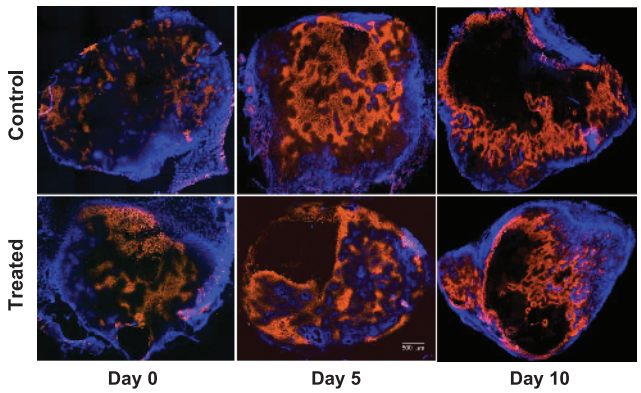

Figure 5. Images of the tumor sections from six representative animals and time points stained using Hoechst and pimonidazole. Blue marks Hoechst-33342 fluorescence, whereas the orange-stained areas indicate pimonidazole binding. The percent hypoxic fractions on days 0, 5, and 10 were 5%, 33%, and 41%, respectively, for the control tumors and 22%, 49%, and 11%, respectively, for the treated tumors. The dark regions were either necrotic or nonperfused, and the percent necrotic fractions were assessed using H&E stains (data not shown). Scale bar, 500 μm.

assess that the trends displayed by the optical and IHC end points are similar across time, multivariate statistical models were built in an additive fashion to determine the effect of time (day) and treatment for both groups of data. These analyses indicated that the hypoxic fractions and dHb concentrations required the addition of quadratic polynomial terms ($P < .001$) to fit the temporal variations of the data, whereas the necrotic fractions and the $\langle\mu_s'\rangle$ required cubic-order polynomial ($P < .001$) terms to capture temporal variations in these parameters across time. However, neither the hypoxic fraction nor the necrotic fraction (or their optical analogues) showed statistically significant differences in the temporal trends between the treated and the control groups. A summary of the conclusions of the multivariate statistical models is as follows: the temporal trends between the hypoxic fractions and dHb concentrations and between the necrotic fractions and the $\langle\mu_s'\rangle$ were statistically similar, but no effect of treatment was perceived across any of these parameters in this smaller cohort of animals that was observed in the larger cohort (Figure 4).

Given the linear increase with time in $\langle\mu_s'\rangle$ and tumor volumes seen in Figure 4, *E* and *F*, and the similarity of temporal trends in $\langle\mu_s'\rangle$ and necrotic fractions seen in Figure 6, *C* and *D*, we evaluated the relationship between $\langle\mu_s'\rangle$ with both necrotic fraction and tumor volume in the treated and control animals through two-dimensional scatter plots. Figure 7 shows the relationship between the estimated $\langle\mu_s'\rangle$ and necrotic fraction for the treated animals (Figure 7*A*, *blue symbols*) and control animals (Figure 7*B*, *red symbols*). It should be noted that the data in these figures are obtained only from the animals that underwent IHC. Figure 7, *C* and *D*, shows the dependence of $\langle\mu_s'\rangle$ on the tumor volume for all treated and control animals, respectively. The *dashed lines* in each of these figures are the lines of regression and show that the extracted $\langle\mu_s'\rangle$ was related linearly related to both the necrotic fraction and tumor volume in both the treated and

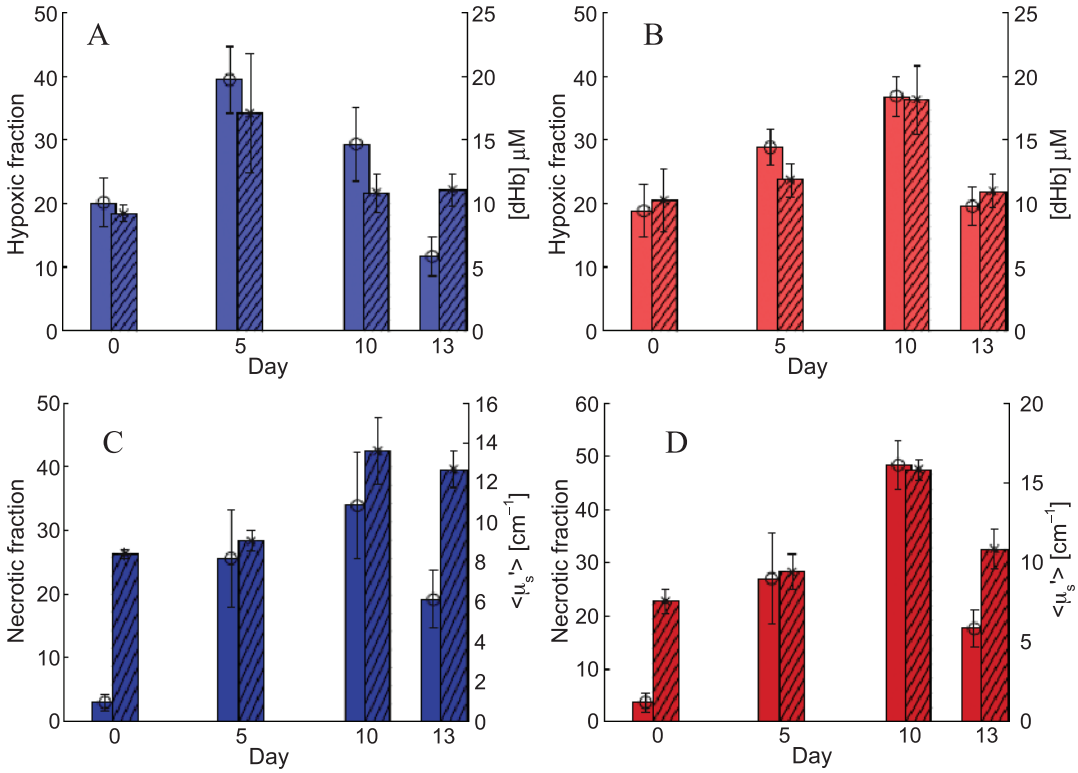

Figure 6. Comparisons between the optical and IHC end points. (A and B) Changes in mean hypoxic fractions assessed using IHC (plain bars, left *y*-axis) and corresponding optical dHb measurements (hatched bars, right *y*-axis) for the treated (light blue, A) and control (light red, B) animals. (C) Changes in histologically assessed necrotic fraction (plain bars, left *y*-axis) and optically determined $\langle\mu_s'\rangle$ (hatched bars, right *y*-axis) for the treated group (dark blue). (D) The same data for the control group (dark red). The optical data shown here were obtained from the same animals used for IHC (five per group) per time point. Error bars indicate SEs.

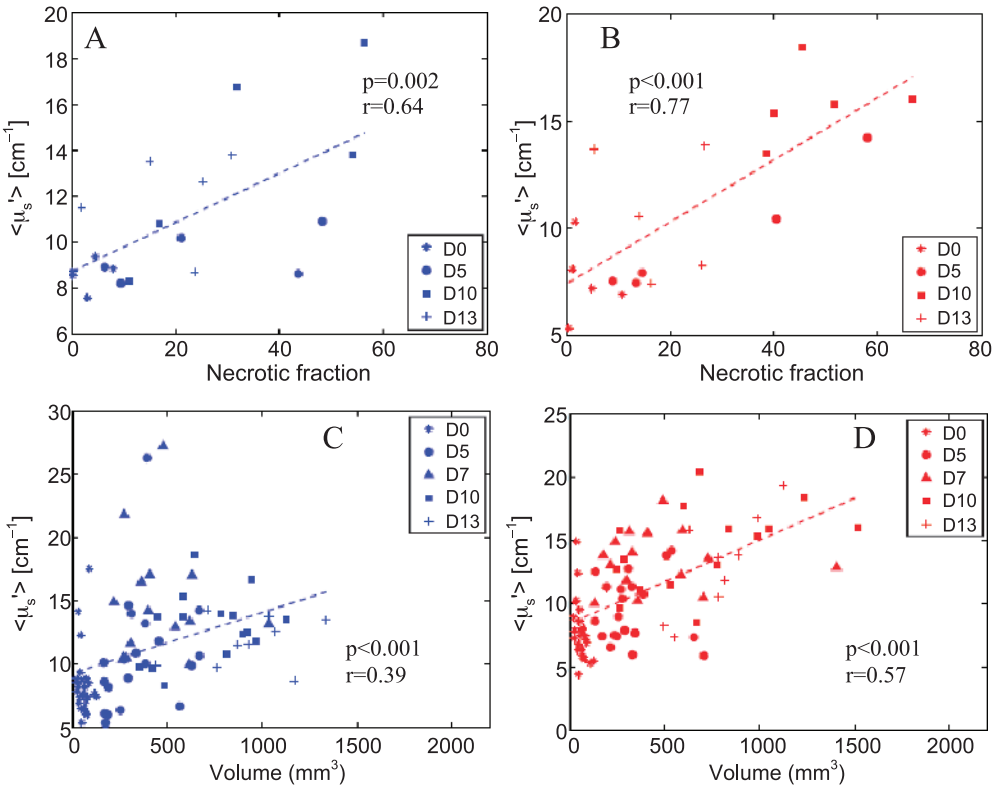

Figure 7. Relationships between the extracted $<\mu_s'>$ with necrotic fraction (A and B) and tumor volume (C and D) for the treated (blue symbols/lines) and control animals (red symbols/lines). The dashed lines indicate the line of regression between the variables on each plot, whereas the *P* value and the regression coefficient are shown on each plot. Different symbols represent data obtained on different days and are shown in the figure legend.

the control groups, although these relationships were marginally stronger in the control animals.

Discussion

Scientific investigators have recognized the need for being able to noninvasively and repeatedly interrogate the underlying physiology and pathology of tumors *de novo* and in response to therapy. This recognition, in large part, has stimulated the revolution in molecular and functional imaging in small animals using micro–computed tomography, micro-PET, high-resolution MR, and ultrasound. Whereas all of these methods can yield important information about the tumor, they are very expensive and time-consuming and may require the use of multiple modalities to capture the full spectrum of relevant biomarkers. Optical techniques are well suited to dynamically and repeatedly monitor physiological and morphologic changes in small animal tumor models. One could easily obtain simple yet quantitative spectroscopic end points along with tumor dimensions and body weight, and these measurements can then be used in the final analysis of treatment results to drive the selection and timing for further detailed studies using micro–computed tomography, MRI, or IHC, for example.

In this study, we measured changes in tumor physiology and morphology optically across a period of 2 weeks in a nude mouse model bearing 4T1 tumor treated with MTD DOX. The optical end points showed that the HbO_2 concentration and tumor SO_2 in the treated animals were statistically significantly increased after drug administration relative to the untreated controls. Furthermore, there was an overall decrease in the mean first-order temporal trend for dHb concentration in the treated group, whereas it was increased for the animals in the control group (although these differences were not statistically significant). Overall changes in THb and $<\mu_s'>$ were nearly identical for both control and treated animals, similar to the trends observed in measured gross tumor volumes.

Previously reported results are consistent with the optically based findings in this study. Oxygenation measurements of untreated 4T1 tumors using hyperspectral imaging in a mouse window chamber model have previously shown that these tumors became progressively hypoxic over time [31] as was observed in our study. It has also been shown that tumor cells treated with 10 mg/kg DOX in mice bearing 16/C mammary tumors showed improved oxygenation as soon as 4 hours after treatment [23]. Another study assessed changes in tumor hypoxia in rats bearing 9L gliosarcoma tumors using a Po_2 electrode 24 hours after administration of DOX treatment and reported that the treatment improved the overall median Po_2 to 5.2 mm Hg relative to a pretreatment median Po_2 value of 1.4 mm Hg [32]. It has also been reported that untreated 4T1 tumors in BALB/c mice showed large areas of necrosis in the central tumor core 2 to 4 weeks after tumor cell implantation [33] and that MTD DOX (6.25 mg/kg) administration to rats bearing MTLn3 mammary adenocarcinomas caused more than 75% of the area of tumor sections to become necrotic 48 hours after treatment [34]. Observations of increased angiogenesis within untreated 4T1 tumor models in mice have been reported previously [35]. However, there are conflicting reports on the antiangiogenic potential of DOX in the literature. Most administrations of DOX use low-dose metronomic schedules, and this dosing routine has been shown to increase angiogenesis in mesenteric tissue of adult male rats [36,37],

whereas another report that detected blood flow and perfusion in mice implanted with the murine squamous cell carcinoma SCCVII observed clear decreases in both blood flow and perfusion in the tumors after administration of DOX [38].

IHC estimates of tumor hypoxia and necrosis that were quantified longitudinally for animals in both groups showed that there were transient increases in tumor hypoxia and necrosis through time for both groups. Given the limited number of animals that were used to obtain these IHC estimates, there were no statistical differences in rates of change in either of these parameters with treatment. However, we were able to show here that there were optical end points that statistically significantly tracked the polynomial time-dependent trends observed in the quantified IHC end points for the corresponding animals. Pairwise comparisons of the extracted $<\mu_s'>$ with necrotic fraction and tumor volume across all animals indicated that there was an increase in tissue scattering with both necrotic fraction and tumor volume. Several factors have been suggested to contribute to an increase or to a decrease in optical scattering in tissue [39]. These include structural changes in the extracellular matrix of the tumor (breakdown of collagen matrix, for instance [40]), changes in water content of tumors (edema) [41], increased mitochondrial differentiation [42], nuclear size and shape, and cell density [43]. Alterations in tumor volume can be affected by cell proliferation and/or cell death (apoptosis, necrosis) and changes in the extracellular matrix density, thus changes in tumor volume or viability can potentially impact tissue optical scattering. Data in Figure 7 suggest that there were alterations in the cellular architecture/density and/or the extracellular matrix with necrosis that influenced tissue scattering. However, the exact basis for these correlations (i.e., which morphologic constituents primarily contribute to these correlations) is unknown at this time and will be the subject of future exploratory studies. These data suggest that it may be possible to track tissue necrotic fraction *in situ* using the optical end point of $<\mu_s'>$.

This study shows that reflectance spectroscopy has the potential to dynamically monitor changes in tumor physiology and morphology in preclinical models and can therefore be used as a tool for longitudinal drug screening studies, for instance, to perhaps determine important time points at which there are maximal differences in tumor physiological end points between animals receiving different treatments, which might or might not be captured accurately through standard tumor growth assays. This was clearly demonstrated by our study: the optical measurements showed that treatment with DOX increased tumor oxygenation, which was consistent with previously reported studies. However, tumor volume measurements showed no effect of the drug on controlling the rate of tumor growth. These low-cost, fast optical techniques, in particular, diffuse reflectance spectroscopy, could serve as ideal screening techniques that could shed light about early changes in tumor physiology and morphology with treatments and could provide significant additional insights along with standard growth delay studies. These methods could also reduce the need for large animal numbers in longitudinal studies investigating novel drugs and therapeutics by serving as a guide that could provide specific landmark time points for histologic and/or more sophisticated interventions.

Acknowledgments

The authors thank Laura Moore for help with the data collection and Yulin Zhao for assistance with tumor inoculation.

References

[1] Herzig M and Christofori G (2002). Recent advances in cancer research: mouse models of tumorigenesis. *Biochim Biophys Acta* **1602**, 97–113.
[2] Degenhardt K and White E (2006). A mouse model system to genetically dissect the molecular mechanisms regulating tumorigenesis. *Clin Cancer Res* **12**, 5298–5304.
[3] Cespedes MV, Casanova I, Parreno M, and Mangues R (2006). Mouse models in oncogenesis and cancer therapy. *Clin Transl Oncol* **8**, 318–329.
[4] Tozer GM, Prise VE, Wilson J, Cemazar M, Shan S, Dewhirst MW, Barber PR, Vojnovic B, and Chaplin DJ (2001). Mechanisms associated with tumor vascular shut-down induced by combretastatin A-4 phosphate: intravital microscopy and measurement of vascular permeability. *Cancer Res* **61**, 6413–6422.
[5] Young SL and Chaplin DJ (2004). Combretastatin A4 phosphate: background and current clinical status. *Expert Opin Investig Drugs* **13**, 1171–1182.
[6] Shaked Y, Ciarrocchi A, Franco M, Lee CR, Man S, Cheung AM, Hicklin DJ, Chaplin D, Foster FS, Benezra R, et al. (2006). Therapy-induced acute recruitment of circulating endothelial progenitor cells to tumors. *Science* **313**, 1785–1787.
[7] Moeller BJ, Dreher MR, Rabbani ZN, Schroeder T, Cao Y, Li CY, and Dewhirst MW (2005). Pleiotropic effects of HIF-1 blockade on tumor radiosensitivity. *Cancer Cell* **8**, 99–110.
[8] Hockel M and Vaupel P (2001). Tumor hypoxia: definitions and current clinical, biologic, and molecular aspects. *J Natl Cancer Inst* **93**, 266–276.
[9] Vaupel P and Harrison L (2004). Tumor hypoxia: causative factors, compensatory mechanisms, and cellular response. *Oncologist* **9** (Suppl 5), 4–9.
[10] Tatum JL, Kelloff GJ, Gillies RJ, Arbeit JM, Brown JM, Chao KS, Chapman JD, Eckelman WC, Fyles AW, Giaccia AJ, et al. (2006). Hypoxia: importance in tumor biology, noninvasive measurement by imaging, and value of its measurement in the management of cancer therapy. *Int J Radiat Biol* **82**, 699–757.
[11] Seddon BM, Honess DJ, Vojnovic B, Tozer GM, and Workman P (2001). Measurement of tumor oxygenation: *in vivo* comparison of a luminescence fiber-optic sensor and a polarographic electrode in the p22 tumor. *Radiat Res* **155**, 837–846.
[12] Verheij M (2008). Clinical biomarkers and imaging for radiotherapy-induced cell death. *Cancer Metastasis Rev* **27**, 471–480.
[13] Inoue M, Takakuwa T, Minami M, Shiono H, Utsumi T, Kadota Y, Nasu T, Aozasa K, and Okumura M (2008). Clinicopathologic factors influencing postoperative prognosis in patients with small-sized adenocarcinoma of the lung. *J Thorac Cardiovasc Surg* **135**, 830–836.
[14] Minervini A, Di Cristofano C, Gacci M, Serni S, Menicagli M, Lanciotti M, Salinitri G, Rocca CD, Lapini A, Nesi G, et al. (2008). Prognostic role of histological necrosis for nonmetastatic clear cell renal cell carcinoma: correlation with pathological features and molecular markers. *J Urol* **180**, 1284–1289.
[15] Ullrich E, Bonmort M, Mignot G, Kroemer G, and Zitvogel L (2008). Tumor stress, cell death and the ensuing immune response. *Cell Death Differ* **15**, 21–28.
[16] Torigian DA, Huang SS, Houseni M, and Alavi A (2007). Functional imaging of cancer with emphasis on molecular techniques. *CA Cancer J Clin* **57**, 206–224.
[17] Neves AA and Brindle KM (2006). Assessing responses to cancer therapy using molecular imaging. *Biochim Biophys Acta* **1766**, 242–261.
[18] Xu RX and Povoski SP (2007). Diffuse optical imaging and spectroscopy for cancer. *Expert Rev Med Devices* **4**, 83–95.
[19] Richards-Kortum R and Sevick-Muraca E (1996). Quantitative optical spectroscopy for tissue diagnosis. *Annu Rev Phys Chem* **47**, 555–606.
[20] Bigio IJ and Bown SG (2004). Spectroscopic sensing of cancer and cancer therapy: current status of translational research. *Cancer Biol Ther* **3**, 259–267.
[21] Hielscher AH, Bluestone AY, Abdoulaev GS, Klose AD, Lasker J, Stewart M, Netz U, and Beuthan J (2002). Near-infrared diffuse optical tomography. *Dis Markers* **18**, 313–337.
[22] Palmer GM and Ramanujam N (2006). Monte Carlo–based inverse model for calculating tissue optical properties. Part I: Theory and validation on synthetic phantoms. *Appl Opt* **45**, 1062–1071.
[23] Tannock I (1982). Response of aerobic and hypoxic cells in a solid tumor to adriamycin and cyclophosphamide and interaction of the drugs with radiation. *Cancer Res* **42**, 4921–4926.
[24] Arteel GE, Thurman RG, Yates JM, and Raleigh JA (1995). Evidence that hypoxia markers detect oxygen gradients in liver: pimonidazole and retrograde perfusion of rat liver. *Br J Cancer* **72**, 889–895.
[25] Prahl S (2001). Available at: http://omlc.ogi.edu/spectra/hemoglobin/index.html.
[26] van Gemert MJ, Jacques S, Sterenborg HJ, and Star W (1989). Skin optics. *IEEE Trans Biomed Eng* **36**, 1146–1154.
[27] Wang L, Jacques SL, and Zheng L (1995). MCML—Monte Carlo modeling of light transport in multi-layered tissues. *Comput Methods Programs Biomed* **47**, 131–146.

[28] Cheong W-F, Prahl S, and Welch S (1990). A review of the optical properties of biological tissues. *IEEE J Quantum Electron* **26**, 2166–2185.
[29] Diggle PJ (1988). An approach to the analysis of repeated measurements. *Biometrics* **44**, 959–971.
[30] Gart JJ, Krewski D, Lee PN, Tarone RE, and Wahrendorf J (1986). Statistical methods in cancer research. Volume III—The design and analysis of long-term animal experiments. *IARC Sci Publ* **79**, 1–219.
[31] Sorg BS, Moeller BJ, Donovan O, Cao Y, and Dewhirst MW (2005). Hyperspectral imaging of hemoglobin saturation in tumor microvasculature and tumor hypoxia development. *J Biomed Opt* **10**, 44004.
[32] Teicher BA, Holden SA, Ara G, Dupuis NP, Liu F, Yuan J, Ikebe M, and Kakeji Y (1995). Influence of an anti-angiogenic treatment on 9L gliosarcoma: oxygenation and response to cytotoxic therapy. *Int J Cancer* **61**, 732–737.
[33] Tao K, Fang M, Alroy J, and Sahagian GG (2008). Imagable 4T1 model for the study of late stage breast cancer. *BMC Cancer* **8**, 228.
[34] Toyota N, Strebel FR, Stephens LC, Matsuda H, Oshiro T, Jenkins GN, and Bull JM (1998). Therapeutic efficacy and apoptosis and necrosis kinetics of doxorubicin compared with cisplatin, combined with whole-body hyperthermia in a rat mammary adenocarcinoma. *Int J Cancer* **76**, 499–505.
[35] Shan S, Sorg B, and Dewhirst MW (2003). A novel rodent mammary window of orthotopic breast cancer for intravital microscopy. *Microvasc Res* **65**, 109–117.
[36] Albertsson P, Lennernas B, and Norrby K (2003). Chemotherapy and antiangiogenesis: drug-specific effects on microvessel sprouting. *APMIS* **111**, 995–1003.
[37] Albertsson P, Lennernas B, and Norrby K (2006). On metronomic chemotherapy: modulation of angiogenesis mediated by VEGE-A. *Acta Oncol* **45**, 144–155.
[38] Durand RE and LePard NE (1994). Modulation of tumor hypoxia by conventional chemotherapeutic agents. *Int J Radiat Oncol Biol Phys* **29**, 481–486.
[39] Mourant JR, Freyer JP, Hielscher AH, Eick AA, Shen D, and Johnson TM (1998). Mechanisms of light scattering from biological cells relevant to noninvasive optical-tissue diagnostics. *Appl Opt* **37**, 3586–3593.
[40] Chang VT, Cartwright PS, Bean SM, Palmer GM, Bentley RC, and Ramanujam N (2009). Quantitative physiology of the precancerous cervix *in vivo* through optical spectroscopy. *Neoplasia* **11**, 325–332.
[41] Cerussi AE, Shah N, Hsiang D, Durkin A, Butler J, and Tromberg B (2006). *In vivo* absorption, scattering, and physiologic properties of 58 malignant breast tumors determined by broadband diffuse optical spectroscopy. *J Biomed Opt* **11**, 044005.
[42] Beauvoit B, Kitai T, and Chance B (1994). Contribution of the mitochondrial compartment to the optical properties of the rat liver: a theoretical and practical approach. *Biophys J* **67**, 2501–2510.
[43] Drezek R, Guillaud M, Collier T, Boiko I, Malpica A, Macaulay C, Follen M, and Richards-Kortum R (2003). Light scattering from cervical cells throughout neoplastic progression: influence of nuclear morphology, DNA content, and chromatin texture. *J Biomed Opt* **8**, 7–16.